MDPI

Article

A Combination of EPR, Microscopy, Electrophoresis and Theory to Elucidate the Chemistry of W- and N-Doped TiO$_2$ Nanoparticle/Water Interfaces

Sam Gorman [1], Kirstie Rickaby [1], Li Lu [2], Christopher J. Kiely [2], Donald E. Macphee [1] and Andrea Folli [3,*]

[1] Department of Chemistry, University of Aberdeen, Meston Building, Meston Walk, Aberdeen AB24 3UE, UK; r04sg16@abdn.ac.uk (S.G.); kirstie.rickaby@outlook.com (K.R.); d.e.macphee@abdn.ac.uk (D.E.M.)
[2] Whitaker Laboratory, Department of Materials Science and Engineering, Lehigh University, 5 East Packer Ave, Bethlehem, PA 18015, USA; li.lu@alum.lehigh.edu (L.L.); chk5@lehigh.edu (C.J.K.)
[3] School of Chemistry, Cardiff University, Main Building, Park Place, Cardiff CF10 3AT, UK
* Correspondence: follia@cardiff.ac.uk

Abstract: The doping of TiO$_2$-based nanomaterials for semiconductor-sensitised photoreactions has been a practice extensively studied and applied for many years. The main goal remains the improvement of light harvesting capabilities under passive solar irradiation, that in the case of undoped TiO$_2$ is limited and restricted to relatively low latitudes. The activity and selectivity of doped TiO$_2$ photocatalysts are generally discussed on the basis of the modified band structure; energetics of intrinsic or extrinsic band gaps including trapping states; redox potentials of band edges, including band bending at solid/fluid interfaces; and charge carriers scavenging/transfer by/to adsorbed species. Electron (and hole) transfer to adsorbates is often invoked to justify the formation of highly reactive species (e.g., HO$^\bullet$ from water); however, a complete description of the nanoparticle surface chemistry dictating adsorption/desorption events is often missing or overlooked. Here, we show that by employing a surface electrochemical triple-layer (TLM) approach for the nanoparticles/water interface, in combination with electron paramagnetic resonance spectroscopy (EPR), transmission electron microscopy and electrophoretic measurements, we can elucidate the surface chemistry of doped TiO$_2$ nanoparticles and link it to the nature of the dopants. Exemplifying it for the cases of undoped, as well as W- and N-doped and codoped TiO$_2$ nanoparticles, we show how surface charge density; surface, Stern and ζ potentials; surface acidity constants; and speciation of surface sites are influenced by the nature of the dopants and their loading.

Keywords: electron paramagnetic resonance; semiconductor photocatalysis; TiO$_2$; colloidal chemistry; solid-liquid interface; metal oxides; surface chemistry; surface charge density; zeta potential; isoelectric point; pH of zero charge

1. Introduction

The doping of TiO$_2$ nanomaterials for semiconductor-sensitised photoreactions has been a practice extensively studied and applied for many years; the use of undoped TiO$_2$ in passive solar applications is limited and restricted to relatively low latitudes [1]. The improvement of light harvesting capabilities under passive solar irradiation as well as the enhancement of activity and selectivity of TiO$_2$-sensitised photoreactions remain the main goals for which this practice is employed. Doping strategies have been largely explored through the last three decades, including self-doping [2–4]; non-metal doping [5–10]; transitional metal doping [11–24]; metal, non-metal codoping [25–33]; and rare-earth metal doping [34,35]. The literature cited here is only representative of a few examples and by no means exhaustive. These works show that dopants can play a pivotal role in stabilising phases otherwise thermodynamically unstable, altering the electronic configuration and energetics of the host lattice, and therefore governing the magnetic, optical as well as

chemical and catalytic properties of the host metal oxide. In the case of transition metal dopants, their partially filled d-orbitals allow for a series of new energy levels below the conduction band edge of the host semiconductor to be accessible. Often, the result is a red shift of the band-gap transition and a modulation of the semiconductor Fermi level. Furthermore, these new energy levels can alter the charge carrier equilibrium concentration by serving as electron–hole trapping centres, potentially suppressing charge carrier recombination (if both electron and hole are separately trapped) or enhancing charge carrier recombination (if both electron and hole are trapped by the same centre or, in the absence of charge scavengers, one of the two charge carriers is trapped while the other is not). An example of the latter case is elegantly demonstrated by D'Arienzo et al. [36] using N-doped TiO_2. These authors found that dopant-induced recombination events can completely counterbalance the additional charge separation resulting from successful sensitisation of the photocatalyst with visible light photons [36]. Electron trapping generally occurs at a much faster rate than hole trapping, and in most of the cases the net result is a reduction of the oxidation state of the metal ions in the TiO_2 crystal lattice.

Electron Paramagnetic Resonance (EPR) spectroscopy has proven to be a technique of supreme elegance, sensitivity and wealth of information for analysing electron trapping as well as electron transfer events, the chemical and crystallographic nature of the trapping centres and reduced metal ions in doped TiO_2, and it has proved imperative when designing high performance photocatalysts and semiconductor sensitisers.

Here, we show that EPR can also be used in combination with electron microscopy, electrophoresis and colloidal chemistry theory to provide unique insights into the nature of colloidal nanoparticles doped TiO_2 surfaces and aqueous interface chemistry. Structural and thermodynamic parameters that are derived allow to interpret adsorption/desorption mechanisms of reactive substrates in semiconductor photocatalysis, i.e., details that are often overlooked when assessing photocatalytic activity/selectivity of semiconductor sensitised photoreactions using doped TiO_2 nanoparticles. In this study, we are presenting an interpretation of the metal oxide/electrolyte (aqueous solution) interface for W and N codoped TiO_2 and comparing it to the case of undoped TiO_2 as well as monodoped W or N TiO_2 to ascertain the role of the single dopants in conditioning the surface/interface chemistry. EPR data are coupled to experimental and simulated data of surface charge densities, Stern and electrokinetic potentials which are analysed and interpreted using the interfacial model proposed by Blesa and Kallay [37].

2. Theoretical Description and Simulation of the 2-pK Charging Triple-Layer Model (2-pK TLM) of the Oxide/Electrolyte Interface
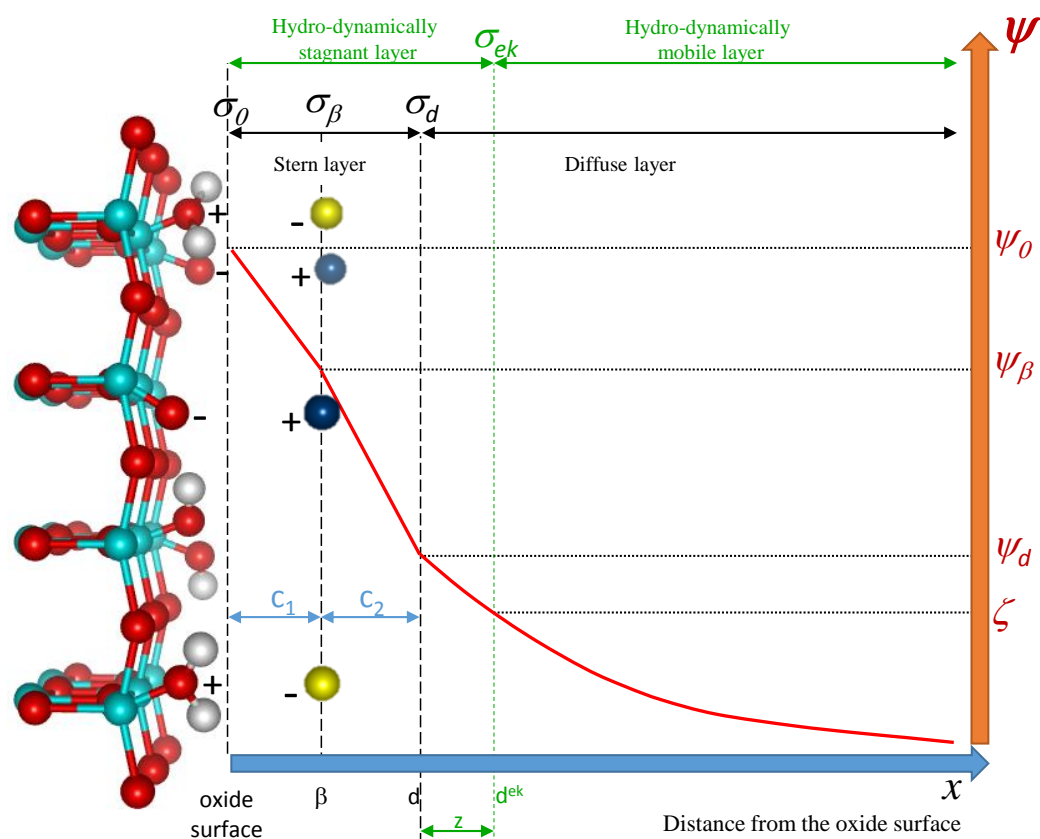
2.1. Theoretical Description

A typical diagram of the triple-layer model (TLM) is shown in Figure 1. On the basis of the theoretical approach proposed by Piasecki et al. [38], SO^- is considered to be the free surface site (i.e., unoccupied surface oxygen), the concentration of which is denoted by $[SO^-]$. S is used to denote a surface metal atom. The potential determining ions, i.e., H^+, together with the ions C^+ and A^- of the supporting electrolyte, can form surface complexes denoted as SOH, SOH_2^+, SO^-C^+ and $SOH_2^+A^-$ with concentrations represented by $[SOH]$, $[SOH_2^+]$, $[SO^-C^+]$ and $[SOH_2^+A^-]$, respectively. This chemistry is possible due to the amphoteric character of the surface SOH groups:

$$SOH_2^+ \rightleftharpoons SOH + H^+ \qquad\qquad K_{a1}^{int} \qquad\qquad (1)$$

$$SOH \rightleftharpoons SO^- + H^+ \qquad\qquad K_{a2}^{int} \qquad\qquad (2)$$

and the counterions association with the charged surface sites, i.e., adsorption of counterions in the Stern layer. K_{an}^{int} represent the dissociation constants of protonated surface sites.

$$SOH + C^+ \rightleftharpoons SO^-C^+ + H^+ \qquad\qquad K_C^{int} \qquad\qquad (3)$$

$$SOH_2^+ A^- \rightleftharpoons SOH + H^+ + A- \qquad\qquad K_A^{int} \qquad (4)$$

Figure 1. Schematic representation of the charge densities and potentials in a triple-layer model (TLM) configuration with three charged planes: metal oxide surface; β plane, where associated counter ions are located; d plane, onset of the diffuse layer. The 2 different pKs are a consequence of the amphoteric character of the surface hydroxyl groups. In the figure, the hydro-dynamically stagnant and mobile layers are also depicted in green.

Association of counterions can be symmetric or asymmetric. Reactions (1)–(4) are characterised by the following equilibrium constants:

$$K_{a1}^{int} = \frac{[SOH]a_H}{[SOH_2^+]} \exp\left(-\frac{F\psi_0}{RT}\right) \qquad (5)$$

$$K_{a2}^{int} = \frac{[SO^-]a_H}{[SOH]} \exp\left(-\frac{F\psi_0}{RT}\right) \qquad (6)$$

$$K_C^{int} = \frac{[SO^-C^+]a_H}{[SOH]a_C} \exp\left(-\frac{F(\psi_0 - \psi_\beta)}{RT}\right) \qquad (7)$$

$$K_A^{int} = \frac{[SOH]a_H a_A}{[SOH_2^+A^-]} \exp\left(-\frac{F(\psi_0 - \psi_\beta)}{RT}\right) \qquad (8)$$

In the above equations, a_j are the activities of the species j in the bulk solution ($j = H, C, A$, protons and ions of the supporting electrolyte) in contact with the oxide surface, F the Faraday constant, R the universal gas constant and T the absolute temperature. ψ_0 and ψ_β are the potentials at the metal oxide surface and β plane, respectively. The TLM can be seen as a series of electrical capacitors at constant capacitance. The first capacitor is defined by the metal oxide surface and the β plane, and it is characterised by the capacitance c_1.

The TLM assumes an additional potential drop (before the diffuse layer) [37] represented by a second capacitor with capacitance c_2, defining the onset of the diffuse layer. The introduction of this second capacitor does not reflect the existence of another charged plane; as Bleasa and Kallay [37] clearly pointed out, the capacitance c_2 is simply introduced to improve the fit. For an exhaustive discussion of the model and the significance of the capacitors, the reader should refer to the original paper of Blesa and Kallay [37]. Briefly, the fundamental assumption for the second capacitance is that the solvated ions from the diffuse layer cannot approach the β plane given their large size caused by the solvation shell. Therefore, two defined and different capacitances (in the Stern layer) hold only if the associated ions (determining the distance of the β plane) are stripped by their solvation shell (Stern's assumption for metal surfaces). Tejedor-Tejedor and Anderson [39], however, could not find proof for this desolvation effect in metal oxide systems. Furthermore, if counterions only approach the d plane but not β plane, then a potential drop between the β and d cannot occur.

The final capacitor is the diffuse layer capacitor, defined between the d plane and the distribution of charges in the plane of the bulk side and characterised by the capacitance c_d. The latter is not constant and depends on the potential, ionic strength, temperature and permittivity; it can be derived by the Gouy–Chapman theory. Given the type of metal oxides involved and the experimental conditions adopted in the present work, the potential profile of the TLM can be simplified with no intermediate potential drop between the metal surface and d plane. This rationalises the TLM to a simpler original Stern model. Mathematically, this corresponds to assuming the capacitance $c_2 \to \infty$. The expressions for the capacitances c_1 and c_2 are

$$\psi_0 - \psi_\beta = \frac{\sigma_0}{c_1} \tag{9}$$

$$\psi_\beta - \psi_d = -\frac{\sigma_d}{c_2} \tag{10}$$

where σ_0 and ψ_0 are the charge density and potential of the metal oxide surface, ψ_β the potential at the β plane, σ_d and ψ_d the charge density and potential at the d plane. Given that $c_2 \to \infty$, $\psi_\beta = \psi_d$. ψ_d is commonly referred to as Stern potential.

The Gouy–Chapman theory of the diffuse part of the interfacial layer can be used to determine the Stern potential as

$$\psi_d = \frac{2RT}{|z|F} \ln \left[\frac{-\sigma_d}{(8\epsilon_0\epsilon_r RTI)^{1/2}} + \left(\frac{\sigma_d^2}{8\epsilon_0\epsilon_r RTI} + 1 \right)^{1/2} \right] \tag{11}$$

where ϵ_r is the relative permittivity of the solvent (in this case water), ϵ_0 is the permittivity of free space and I is the ionic strength of the solution in $\mathrm{mol\,m^{-3}}$. Substituting Equations (9) and (10) in Equation (11), the surface potential ψ_0 can be derived:

$$\psi_0 = \frac{\sigma_0}{c_1} - \frac{\sigma_d}{c_2} + \frac{2RT}{|z|F} \ln \left[\frac{-\sigma_d}{(8\epsilon_0\epsilon_r RTI)^{1/2}} + \left(\frac{\sigma_d^2}{8\epsilon_0\epsilon_r RTI} + 1 \right)^{1/2} \right] \tag{12}$$

2.2. Simulation of Surface Charge Density, $\sigma_0(pH)$ and Surface Site Speciation

For the simulation exercise, reactions (1)–(4) can be rewritten as formation reactions of the surface complexes from the free sites, potential determining ions and counterions:

$$\mathrm{SO^- + H^+ \rightleftharpoons SOH} \qquad\qquad K_0 \tag{13}$$

$$\mathrm{SO^- + 2\,H^+ \rightleftharpoons SOH_2^+} \qquad\qquad K_+ \tag{14}$$

$$\mathrm{SO^- + C^+ \rightleftharpoons SO^-C^+} \qquad\qquad K_C \tag{15}$$

$$\mathrm{SO^- + 2\,H^+ + A^- \rightleftharpoons SOH_2^+A^-} \qquad\qquad K_A \tag{16}$$

where equilibrium constants are, respectively,

$$K_0 = \frac{1}{K_{a2}^{int}} = \frac{[SOH]}{[SO^-]a_H}\exp\left(\frac{F\psi_0}{RT}\right) \tag{17}$$

$$K_+ = \frac{1}{K_{a1}^{int}K_{a2}^{int}} = \frac{[SOH_2^+]}{[SO^-]a_H^2}\exp\left(\frac{2F\psi_0}{RT}\right) \tag{18}$$

$$K_C = \frac{K_C^{int}}{K_{a2}^{int}} = \frac{[SO^-C^+]}{[SO^-]a_C}\exp\left(\frac{F\psi_\beta}{RT}\right) \tag{19}$$

$$K_A = \frac{1}{K_{a2}^{int}K_A^{int}} = \frac{[SOH_2^+A^-]}{[SO^-]a_H^2 a_A}\exp\left(\frac{F(2\psi_0 - \psi_\beta)}{RT}\right) \tag{20}$$

The total surface site density is the sum of the concentrations of all the species present on the oxide surface, being

$$N_s = [SO^-] + [SOH] + [SOH_2^+] + [SO^-C^+] + [SOH_2^+A^-] \tag{21}$$

therefore dividing both numerator and denominator of the right-hand sides of Equations (17)–(20) by N_s, the concentrations become the fractional surface coverage θ, which can then be expressed as

$$\frac{\theta_0}{\theta_-} = K_0 a_H \exp\left(-\frac{F\psi_0}{RT}\right) = K_0 \exp\left(-\frac{F\psi_0}{RT} - 2.303 pH\right) = K_0 f_0 \tag{22}$$

$$\frac{\theta_+}{\theta_-} = K_+ a_H^2 \exp\left(-\frac{2F\psi_0}{RT}\right) = K_+ f_0^2 \tag{23}$$

$$\frac{\theta_C}{\theta_-} = K_C a_C \exp\left(-\frac{F\psi_\beta}{RT}\right) = K_C a_C \exp\left(-\frac{F\psi_0}{RT} + \frac{F\sigma_0}{RTc_1}\right) = K_C f_C \tag{24}$$

$$\frac{\theta_A}{\theta_-} = K_A a_H^2 a_A \exp\left(-\frac{F(2\psi_0 - \psi_\beta)}{RT}\right) = K_A a_A \exp\left(-\frac{F\psi_0}{RT} - \frac{F\sigma_0}{RTc_1} - 4.606 pH\right) = K_A f_A \tag{25}$$

where Equations (24) and (25) also include Equation (9). With some simple algebra, one can demonstrate that

$$\theta_- = 1 - \sum_i \theta_i = \frac{1}{1 + \sum_i K_i f_i} \quad \text{with} \quad i = 0, +, C, A \tag{26}$$

Substituting Equation (26), the system of nonlinear Equations (22)–(25) can be generalised as

$$\theta_i = \frac{K_i f_i}{1 + \sum_i K_i f_i} \quad \text{with} \quad i = 0, +, C, A \tag{27}$$

representing a Langmuir-like form of the individual ion adsorption isotherms. The Coulombic definition of the surface charge density σ_0 can be easily deduced as the sum of all the charges present on the surface of the metal oxide, thus

$$\sigma_0 = F([SOH_2^+] + [SOH_2^+A^-] - [SO^-] - [SO^-C^+]) = N_s F(\theta_+ + \theta_A - \theta_- - \theta_C) \tag{28}$$

Substituting Equations (27) and (26) in Equation (28), the following expression for the surface charge density can be derived:

$$\sigma_0 = N_s F \frac{K_+ f_+ + K_A f_A - K_C f_C - 1}{1 + \sum_i K_i f_i} \tag{29}$$

Solving numerically the nonlinear Equation (29), the charge density of the metal oxide surface can be simulated for each value of pH, and consequently the fractional coverages of the different surface complexes can be derived as a function of the pH too.

2.3. Simulation of Electrokinetic Potential, ζ(pH)

The potential in the diffuse layer as a function of the distance from the d plane (exponential decay of $\psi(x')$ with $x' = x - d$, see Figure 1), can be derived as a solution of the Poisson–Boltzmann equation within the domain of the Debye–Hückel approximation ($\psi(0)$ assumed to be small relative to $k_B T$) [37].

$$\psi(x') = \frac{2RT}{F} \ln \frac{1 + g_d \exp(-\kappa x')}{1 - g_d \exp(-\kappa x')} \tag{30}$$

where g_d is a function of the Stern potential $\psi_d(\text{pH})$:

$$g_d = \frac{\exp(F\psi_d/2RT) - 1}{\exp(F\psi_d/2RT) + 1} \tag{31}$$

and κ, dependent on the ionic strength and temperature only, is the Debye–Hückel length or reciprocal of the double layer thickness, i.e., the distance from the surface at which the electrical potential drops to roughly $1/3$ the value at the surface and beyond which the charges are electrically screened:

$$\kappa = \left(\frac{2F^2 I}{\epsilon_r \epsilon_0 RT} \right)^{\frac{1}{2}} \tag{32}$$

The simulated values of $\psi_d(\text{pH})$ from the previous section can therefore be fed into Equation (31) and $\psi(x')$ profiles over a given pH range at a given distance x' simulated too. The profile that best fits the experimental values of ζ is then chosen as ζ-potential profile. For low values of surface potentials and low concentrations of electrolytes in the bulk phase, the identity $\zeta \equiv \psi_d$ has been commonly accepted in the literature.

3. Materials and Methods

3.1. Synthesis

All the doped TiO$_2$ photocatalysts used in this work were synthesised according to synthetic procedures described in our previous works [30–32,40].

A commercially available, undoped anatase TiO$_2$, i.e., Tronox CristalACTiV$^{\text{TM}}$ PC-105, was used as a reference for comparison (Tronox, Stallingborough Grimsby, North East Lincolnshire, United Kingdom).

3.2. Aberration Corrected Scanning Transmission Electron Microscopy (STEM)

Samples for examination by scanning transmission electron microscopy (STEM) were prepared by dispersing the dry catalyst powder onto a holey carbon film supported by a 300 mesh copper TEM grid. STEM high-angle annular dark-field (HAADF) images of the samples were obtained using an aberration corrected JEM ARM-200CF STEM operating at 200 kV (JEOL, Peabody, MA, USA).

3.3. Electron Paramagnetic Resonance (EPR) Spectroscopy

The X-band CW-EPR spectra were recorded on a Bruker Elexsys E500 (Bruker Biospin, Rheinstetten, Germany) spectrometer equipped with an Oxford Instruments liquid-helium cryostat (Oxford Instruments, Abingdon, United Kingdom) and a Bruker ER4122 SHQE-W1 super high Q resonator (Bruker Biospin, Rheinstetten, Germany), operating at 50 K.

Before each measurement, the samples were evacuated for at least 12 h at 393 K and under dynamic vacuum, ca. 10^{-4} bar. Spectra were recorded in the absence of ultra

band gap irradiation. Experimental spectra were simulated and fitted using the EasySpin MATLAB® toolbox [41].

3.4. Electrolyte and Mass Titrations

The experimental evaluation of the pH of zero charge (PZC) and the surface charge density was conducted according to the electrolyte titration method described in Folli et al. [42] and the mass titration method described in Preočanin and Kallay [43] as well as Reymond et al. [44]. Electrolyte as well as mass titrations were conducted in solutions of $NaNO_3$ at a constant ionic strength of $10^{-2}\,mol\,L^{-1}$. The evaluation of the degree of contamination—essential to correct the PZC derived by mass titration—was conducted according to the method reported in Žalac and Kallay [45].

3.5. Electroacoustics and Laser Doppler Micro-Electrophoresis

ζ potential of solid particle dispersions were measured using a Colloidal Dynamics Zetaprobe analyser™ (Colloidal Dynamics, Ponte Vedra Beach, FL, USA) based on a multi-frequency electroacoustic method, as well as using a Malvern Zetasizer Nano ZS™ (Malvern Panalytical, Malvern, United Kingdom) based on a laser Doppler micro-electrophoretic method. Photocatalyst suspensions were prepared in water at different pH and at a constant ionic strength of $10^{-2}\,mol\,L^{-1}$ through the use of $NaNO_3$ as a supporting electrolyte. In the case of the acoustic method, 1% *w/w* of photocatalyst suspensions were used, while for the laser doppler micro-electrophoretic method, 0.01 % *w/w* of photocatalyst suspensions were used. Before each measurement, the suspensions were stabilised by sonication in ultrasonic bath for 15 min.

4. Results

4.1. Aberration Corrected Scanning Transmission Electron Microscopy (STEM)

Representative high-angle annular dark-field (HAADF) scanning transmission electron microscope (STEM) images of a $Ti_{0.909}W_{0.091}O_2N_x$ sample are shown in Figure 2a,b, in which the W component is readily visible via the mass contrast afforded by this technique. W has a tendency to incorporate substitutionally into the Ti cation sub-lattice sites, in good agreement with neutron diffraction results published elsewhere [31]. At this high concentration however, W also forms discrete clusters on the surface of the nanoparticles (extended bright areas circled in Figure 2a,b), corroborating results from XPS spectroscopy reported in one of our previous papers [31]. Our previous work showed that these clusters are not crystalline WO_3, as anatase TiO_2 was the only crystalline phase detectable by neutron diffraction and no crystalline WO_3 phases were present [31]. Representative low and high magnification HAADF-STEM images of the undoped TiO_2 sample used as a reference throughout this work are shown in Figure 3a,b. Figure 3b is typical of the anatase polymorph of TiO_2 viewed along the [111] projection in which a set of (10-1) planes with d-spacing 0.35 nm is indicated.

4.2. Electron Paramagnetic Resonance (EPR) Spectroscopy

X band (i.e., ~9.5 GHz) continuous wave (CW) EPR spectra of $Ti_{0.909}W_{0.091}O_2N_x$ in the absence of band gap excitation around the free spin region (Figure 2c) is dictated by an adsorbed NO molecule [30,31,46,47], exhibiting the spectrum of an 11 electrons π radical in the adsorbed form characterised by an anisotropic **g** tensor with principal values $g_1 = 2.001, g_2 = 1.998, g_3 = 1.921$ and a **A** tensor with principal values equal to $|A_1^{14N}| < 2.8\,MHz, |A_2^{14N}| = 89.7\,MHz, |A_3^{14N}| = 26.9\,MHz$. The EPR profile is present after the samples were evacuated for at least 12 h at 393 K and under dynamic vacuum, ~10^{-4} bar, signifying that this NO is not adsorbed on the exposed surface of the sample, rather encapsulated in bulk and sub-surface microvoids (or closed pores) generated during the synthetic process, as proved by previous studies on similar systems [47]. This species is due to calcination of the material in air in the presence of nitrogen. The photocatalyst powder needs to be milled at high rpm, in vacuum, for several hours in order to remove this signal [48].

The EPR spectrum is also indicative of an interstitial N chemically bound to a lattice O ion forming a $N_iO^\bullet$ group (an intraband gap NO^{2-} state) with spin density (and therefore the magnetic **g** and **A** tensors) differently polarised depending on whether the $N_iO^\bullet$ is adjacent to a substitutional W^{6+} or not [30,31]. The g and A values for these two species are $g_1 =$ 2.005, $g_2 = 2.004$, $g_3 = 2.003$, $|A_1^{14N}| = 6.5\,\text{MHz}$, $|A_2^{14N}| = 15.7\,\text{MHz}$, $|A_3^{14N}| = 89.7\,\text{MHz}$; and $g_1 = 2.001$, $g_2 = 2.000$, $g_3 = 1.999$, $|A_1^{14N}| = 42.0\,\text{MHz}$, $|A_2^{14N}| = 22.4\,\text{MHz}$, $|A_3^{14N}| = $ 140.1 MHz, $|A_1^{183W}| = 44.8\,\text{MHz}$, $|A_2^{183W}| < 2.8\,\text{MHz}$, $|A_3^{183W}| = 154.1\,\text{MHz}$, respectively. In the absence of band gap excitation (presented in Figure 2c) the signal of $N_iO^\bullet$ is almost negligible (0.40 % and <0.10 %, respectively), and significant spectral contributions are observed only under or post irradiation [30,31]. Given that the doped nanoparticles (which are sensitive to visible light as well as UV) were not left in complete darkness before recording the EPR spectra but had been exposed to ambient light, it is reasonable to assume that a small amount of these paramagnetic species were formed although the particles were not directly photosensitised. For a full description of this species, their photochemistry, and the physical-chemical significance of their spin Hamiltonian parameters (reported in Table 1), the reader should refer to our previous works [30,31].

Table 1. Spin Hamiltonian parameters of the NO centres associated with N doping.

Species	Temp. / K	g_1	g_2	g_3	$\|A_1^{14N}\|$ / MHz	$\|A_2^{14N}\|$ / MHz	$\|A_3^{14N}\|$ / MHz	$\|A_1^{183W}\|$ / MHz	$\|A_2^{183W}\|$ / MHz	$\|A_3^{183W}\|$ / MHz
ads NO	50	2.001 [a]	1.998 [a]	1.921 [a]	<2.8 [b]	89.7 [c]	26.9 [c]			
NO^{2-}	50	2.005 [a]	2.004 [a]	2.003 [a]	6.5 [c]	15.7 [c]	89.7 [c]			
W-NO^{2-}	50	2.001 [a]	2.000 [a]	1.999 [a]	42.0 [c]	22.4 [c]	140.1 [c]	44.8 [c]	<2.8 [b]	154.1 [c]

[a] ±0.001; [b] not accurately measurable on the EPR spectrum; [c] ±2.8 MHz. Simulated spectral linewidths were computed using g strain for g_1, g_2 and g_3, respectively, ads NO: 0.0071 0.0032 0.0022; NO^{2-}: 0.002 0.004 0.003; W-NO^{2-}: 0.003 0.004 0.003.

At higher magnetic fields (Figure 2d), the EPR spectra revealed the presence of two paramagnetic species exhibiting anisotropic **g** tensors with axial symmetry. The first one is characterised by $g_\perp = 1.85$ and $g_\parallel = 1.50$ and can be associated with coordinatively unsaturated W^{5+} species in W_xO_y clusters strongly anchored to the surface of the host crystal [49–51]. The second one is characterised by $g_\perp = 1.80$ and $g_\parallel = 1.64$ and corresponds to W^{5+} in tungsten bronze-like superstructures, weakly bound to the surface of the host crystal [49–51]. This is in line with the presence of surface clusters identified by our HAADF aberration corrected-STEM (Figure 2a,b) as well as our X-ray Photoelectron Spectroscopy investigation that we presented elsewhere [31]. The low principal values of these two tensors are due to the d^1 nature of the W^{5+} ion in combination with the large spin–orbit coupling associated with W^{5+} (i.e., 2700 cm^{-1}) [52]. In Figure 2d, the experimental EPR spectrum is presented with two distinct simulations. The first one considers the orientational distribution of the paramagnetic centres (i.e., W^{5+} ions) in the sample to be isotropic, i.e., all orientations occur with the same probability (inset Figure 2d′ and blue trace simulation), which corresponds to an ordinary powder spectrum. The second one refers to a non-isotropic orientational distribution of the paramagnetic centres in the sample (inset Figure 2d″ and red trace simulation) that was computed according to the function
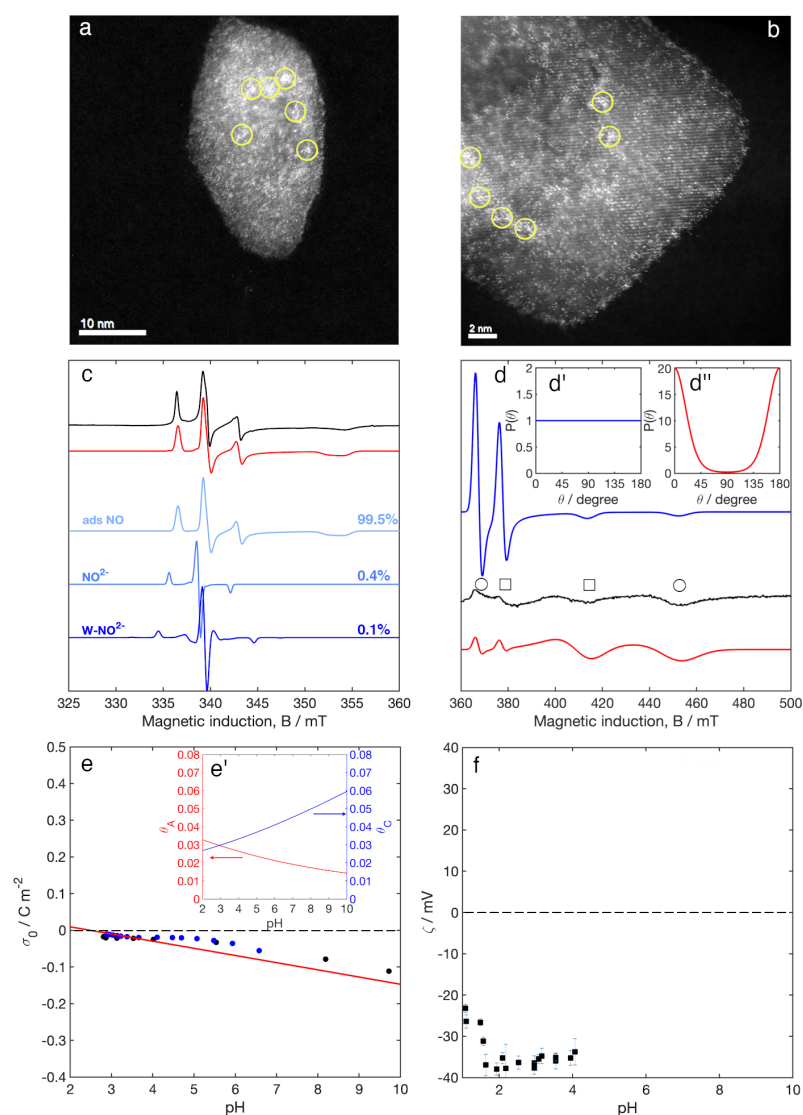
$$P(\theta) = \exp(-U(\theta)) \tag{33}$$

where $U(\theta)$ is a second-order Legendre polynomial in $\cos\theta$ weighted over an "ordering potential", λ.

$$U(\theta) = -\lambda\frac{(3\cos^2\theta - 1)}{2} \tag{34}$$

θ is the angle between the molecular z axis and the static magnetic field.

Figure 2. $Ti_{0.909}W_{0.091}O_2N_x$: (**a**,**b**) Representative HAADF-STEM images. The presence of both substitutional W (brighter dots) and W-containing surface clusters (extended brighter areas highlighted by yellow circles) are evident in the images. (**c**) Experimental (black) and simulated (red) X-band CW EPR spectra recorded at 50 K around the free-spin region. The simulated spectrum is deconvoluted into its three components. The relative spectral contributions are 99.5% adsorbed NO, 0.4% NO^{2-} and ~0.1% $W-NO^{2-}$. (**d**) Experimental (black) and simulated (red and blue) X-band CW EPR spectra measured at 50 K at higher magnetic induction. The relative spectral contributions are 66.7 % W^{5+} in W_xO_y (circles) and 33.3% W^{5+} in W bronzes superstructures (squares). The blue simulation refers to a powder spectrum with orientational probability distribution of the paramagnetic W^{5+} centres given by inset (**d′**). The red simulation refers to a powder spectrum with orientational probability distribution of the paramagnetic W^{5+} centres given by inset (**d″**). The experimental spectra were recorded at 100 kHz field modulation frequency, 0.2 mT field modulation amplitude, 2 µW microwave power, and 72 dB receiver gain. (**e**) Experimental (discrete points) and simulated (red solid line) surface charge density plot at constant ionic strength $I = 10^{-2}$ mol L^{-1}. Both black and blue points are the experimental σ_0 obtained from the mass titrations in Figure S1 and are two different replicates of the same measurement. Inset (**e′**) shows the simulated surface sites speciation relative to the surface site complexes with cations (Na^+) and anions (NO_3^-). (**f**) Experimental electrokinetic (ζ) potential measured at constant ionic strength $I = 10^{-2}$ mol L^{-1} using the laser doppler microelectrophoretic method.
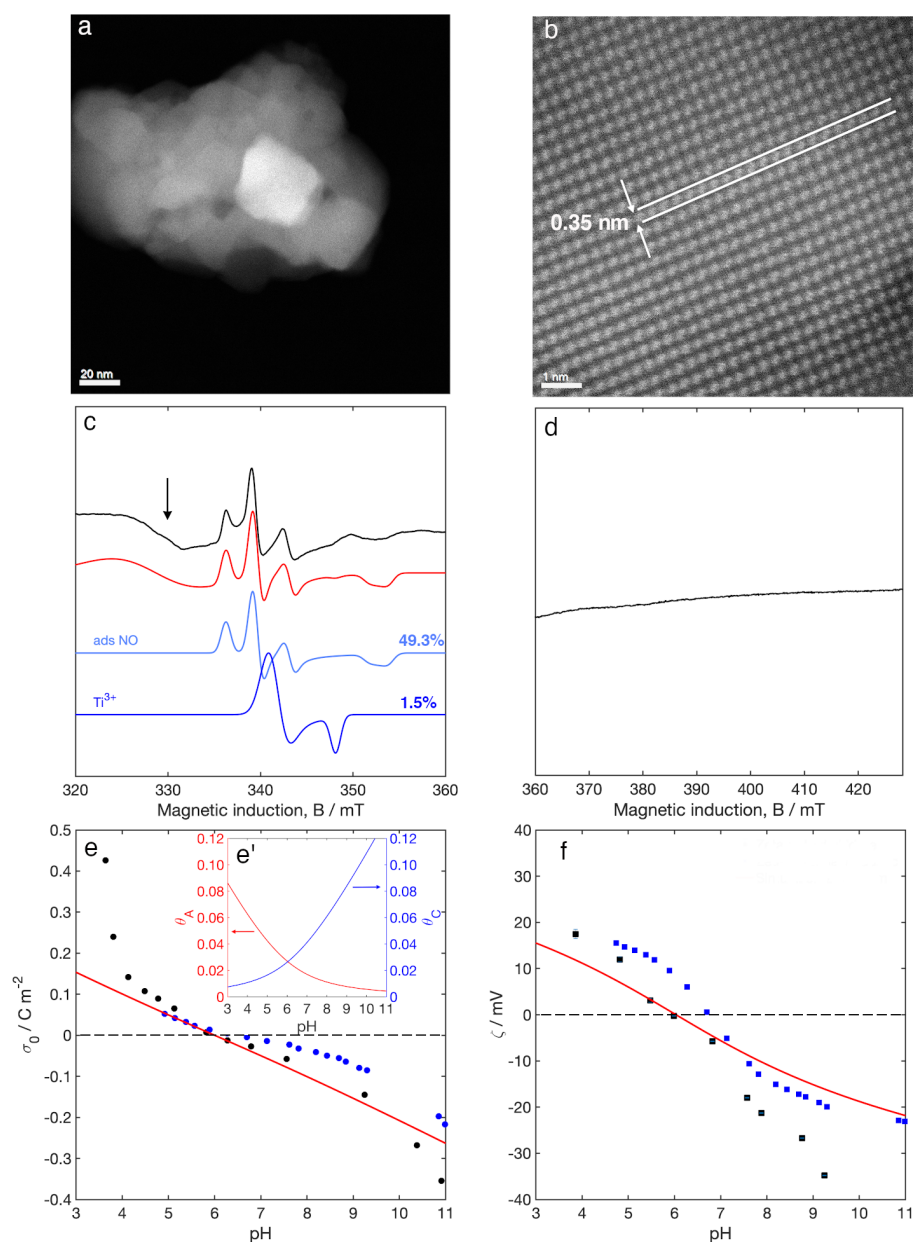
Figure 3. Undoped anatase TiO_2: (**a**,**b**) Representative low and higher magnification HAADF-STEM images. (**c**) Experimental (black) and simulated (red) X-band CW EPR spectra recorded at 50 K around the free-spin region. The two major EPR signals identified are deconvoluted. The relative spectral contributions are 49.3% adsorbed NO and 1.5% Ti^{3+}. The black arrow indicated the broad resonance at approximately $g = 2.05$ with spectral contribution equal to 49.2%. (**d**) Experimental X-band CW EPR spectra measured at 50 K at higher magnetic induction. The experimental spectra were recorded at 100 kHz field modulation frequency, 0.2 mT field modulation amplitude, 2 μW microwave power and 72 dB receiver gain. (**e**) Experimental (discrete points) and simulated (red solid line) surface charge density plot at constant ionic strength $I = 10^{-2}$ mol L^{-1}. The black points are the experimental σ_0 obtained from the mass titrations in Figure S2, while the blue points are the experimental σ_0 obtained according to the electrolyte titration as in Folli et al. [42]. Inset (**e'**) shows the simulated surface sites speciation relative to the surface site complexes with cations (Na^+) and anions (NO_3^-). (**f**) Experimental (discrete points) and simulated (red solid line) electrokinetic (ζ) potential measured at constant ionic strength $I = 10^{-2}$ mol L^{-1}. The black points represent ζ measured using the laser Doppler microelectrophoretic method, while the blue points are ζ measured using the acoustic method.

The experimental spectrum was best simulated and fitted to a non-isotropic orientational distribution of the W^{5+} ions corresponding to a value of λ equal to 3. The spin Hamiltonian parameters of the paramagnetic W^{5+} species can be also found in Table 2. As expected, there is no signal in this portion of the magnetic field in the case of undoped TiO_2, due to the absence of W doping (Figure 3d). Nevertheless, around the free spin region (Figure 3c), undoped TiO_2 exhibited an EPR signal comprising at least three different species. The first one, and with the highest spectral contribution is the same adsorbed NO molecule as described above. Although there is no N doping in this sample, it is not uncommon to find such signal in commercially available undoped TiO_2. The inclusion of NO in the material pores mostly arises from the calcination in air conducted in large rotary kilns on TiO_2 production plants. The spectrum is also likely to contain minor contributions from Ti^{3+} ($g_\perp = 1.988$, $g_\parallel = 1.950$, Table 2) which is often found in TiO_2 due to the trapping of majority carriers (i.e., electrons) without necessarily the presence of trapped holes, unless under UV irradiation (the introduction of a minor contribution of this signal improves the fitting of the simulation). Finally, an unambiguous assignment to the broad resonance around $g \geqslant 2.05$ (indicated by the arrow in Figure 3c) is challenging. Part of this signal could be due to Fe(III) impurities [53] (very common in commercially available anatase TiO_2 samples, especially if produced via the sulphate process). In addition, the signal could also comprise a contribution from the $g_\perp$ of a lattice O^- with significant levels of cationic impurities, causing an increase in the splitting of the π orbitals of the O^- radical, which increase the g values compared to the cases of O^- radical in anatase ($g_\perp = 2.026$) or O^- radical in rutile (multiple $g_\perp$ with the largest values at 2.043) [54–57]. In the simulation, the broad resonance at $g \geqslant 2.05$ was reproduced by means of an effective g value and big enough g strain to account for the signal and the large baseline observed in the experimental spectrum.

Table 2. Spin Hamiltonian parameters of the paramagnetic metal ion centres.

Species	Temp. /K	$g_\perp$	$g_\parallel$
W^{5+} in W_xO_y	50	1.85 [e]	1.50 [e]
W^{5+} in bronze-like superstructures	50	1.80 [e]	1.64 [e]
Ti^{3+}	50	1.988	1.950

[e] ±0.01. Simulated spectral linewidths were computed using g strain for $g_\perp$ and $g_\parallel$, respectively, W^{5+} in W_xO_y: 0.015 0.06; W^{5+} in bronze-like superstructures: 0.015 0.06; Ti^{3+}: 0.014 0.006.

4.3. Surface Charge Density and Electrokinetic Parameters

The surface charge density profiles (σ_0 vs. pH) for $Ti_{0.909}W_{0.091}O_2N_x$ and undoped anatase TiO_2 (reference) measured at constant ionic strength $I = 10^{-2}\,\mathrm{mol\,L^{-1}}$ using $NaNO_3$ as a supporting electrolyte are reported in Figures 2e and 3e, respectively. The mass titration profiles (used to derive σ_0) are reported in Figures S1 and S2. In the course of a mass titration, the pH of the metal oxide dispersion changes gradually, approaching the constant value of pH_∞ in relation to which the absolute value of the slope of the $pH(\gamma)$ function decreases until reaching zero, indicating that the absolute value of the surface charge density approaches zero. According to Equation (35), when a constant value of pH in mass titration of pure metal oxide ($u = 0$) is achieved, the surface charge density σ_0 is equal to zero and pH_∞ is therefore a relatively accurate estimation of the pH of zero charge, pH_{pzc} (also known as point of zero charge), i.e., the pH at which $\sigma_0 = 0$. In the case $u \neq 0$, u must be determined experimentally so that σ_0 can be corrected. In the case of undoped TiO_2, an electrolyte titration was also conducted. The small discrepancy between the pH_{pzc}s obtained via mass titration vs. electrolyte titration is most likely due to the insufficient mass content of titania in the electrolyte titration experiment. It is believed that at higher mass concentrations this discrepancy might disappear, although it is hard to prove experimentally because the dispersion is too dense at high mass concentrations for

carrying out an electrolyte titration. The values of $\sigma_0(\text{pH})$ were calculated from the values of pH_∞ using the formalism proposed by Preočanin and Kallay [43]:

$$\sigma_0 = \frac{Fu}{s} - \frac{F}{s\gamma}\frac{c^\ominus}{y}(10^{-pH_\gamma} - 10^{-pH_{in}} - 10^{pH_\gamma - pK_W^\ominus} + 10^{pH_{in} - pK_W^\ominus}) \tag{35}$$

where γ is the mass concentration of the metal oxide of the specific surface area s. y denotes the activity coefficient of H^+ and OH^- ions in the bulk of the solution given by the extended Debye–Hückel equation and $c^\ominus$ is the standard value of concentration ($c^\ominus = 1\,\text{mol dm}^{-3}$). u is the degree of acid or base contamination and may be obtained from the potentiometric acid–base titration of the concentrated dispersion [45]. Simulation according to the approach described in Section 2 of the surface charge density profile obtained experimentally is also provided. Within the pH range examined σ_0 for $\text{Ti}_{0.909}\text{W}_{0.091}\text{O}_2\text{N}_x$ colloidal nanoparticles remain negative and approaches zero around pH = 2.5. The positive branch of the $\sigma_0(\text{pH})$ curve (i.e., at pH $\leqslant$ 2) was not possible to determine experimentally at $I = 10^{-2}\,\text{mol L}^{-1}$ because it would intrinsically imply ionic strength $\geqslant 10^{-2}\,\text{mol L}^{-1}$. Simulation of the experimental data allowed for an evaluation of the pK_as for reactions (1)–(4) and capacitance c_1 (capacitance of the inner Helmholtz layer). The best fitted parameters are reported in Table 3. To evaluate the extent to which W and N as dopants modify the chemical nature of the TiO_2 nanoparticle surface, the same experimental approach and analysis was conducted on undoped anatase TiO_2. Figure 3e shows the experimental surface charge density obtained using the mass titration method as well as the electrolyte titration method. σ_0 was found to approach 0 at pH = 6 when using the mass titration and slightly above 6 when using the electrolyte titration. The simulated profile of σ_0 vs. pH is also proposed, from which the values of the pK_as for reactions (1)–(4) and capacitance c_1 were evaluated. It is important to highlight that, in order to apply Equation (35) to the potentiometric mass titrations, the value of the the degree of contamination u must be known. The degree of contamination for the undoped anatase TiO_2 used in this work was measured using the procedure proposed by Žalac and Kallay [45] (Figure S3). In the case of $\text{Ti}_{0.909}\text{W}_{0.091}\text{O}_2\text{N}_x$ we applied Equation (35) considering $u = 0$, signifying that the acid-base contaminations of the anatase TiO_2 surface are considered to be the W and N dopants, which therefore cause the shifting of the pH at which $\sigma_0 = 0$ when compared to undoped anatase TiO_2.

Table 3. 2-pK TLM modelled parameters for TiO_2 and $\text{Ti}_{0.909}\text{W}_{0.091}\text{O}_2\text{N}_x$ colloidal nanoparticles aqueous solutions with $I = 10^{-2}\,\text{mol L}^{-1}$ adjusted with NaNO_3.

Sample	pK_{a1}^{int}	pK_{a2}^{int}	pK_C^{int}	pK_A^{int}	c_1	c_2	N_s
					/ F m^{-2}	/ F m^{-2}	/ mol m^{-2}
(anatase) TiO_2	3.20	8.80	5.55	6.45	1.05	inf	1.99×10^{-5}
$\text{Ti}_{0.909}\text{W}_{0.091}\text{O}_2\text{N}_x$	-1.50	4.50	2.00	3.00	0.35	inf	3.00×10^{-5}

The electrokinetic potential, ζ, for $\text{Ti}_{0.909}\text{W}_{0.091}\text{O}_2\text{N}_x$ and TiO_2 is reported in Figures 2f and 3f, respectively. The pH at which $\zeta = 0$, or isoelectric point pH_{iep}, is not achievable within a pH range which allows to have ionic strength $I = 10^{-2}\,\text{mol L}^{-1}$ (i.e., 2 < pH < 12), and it appears to be located at a pH significantly lower than 2. For the case of undoped anatase TiO_2, laser doppler micro-electrophoretic experiments as well as simulations are pointing to a $\text{pH}_{iep} = 6$. A discrepancy is appreciable between the laser doppler micro-electrophoretic experiment and the acoustic one, with the latter indicating a $pH_{iep} = 6.8$. The electrokinetic potential was also measured for a series of other W- and N-doped TiO_2 samples containing different amount of W. In addition, two other samples, one exclusively N-doped, the other one exclusively W doped (10 at.%), were also measured. Results are presented in Figure 4. As evident from Figure 4a–d, the pH_{iep} of the codoped samples approaches the value of undoped TiO_2 as the amount of W loading is reduced.

In addition, the analysis of the monodoped materials revealed that whilst ζ and pH$_{iep}$ for Ti$_{0.909}$W$_{0.091}$O$_2$ are comparable to Ti$_{0.909}$W$_{0.091}$O$_2$N$_x$, there is essentially no significant variation of ζ and pH$_{iep}$ in the solely N doped sample when compared to undoped TiO$_2$.
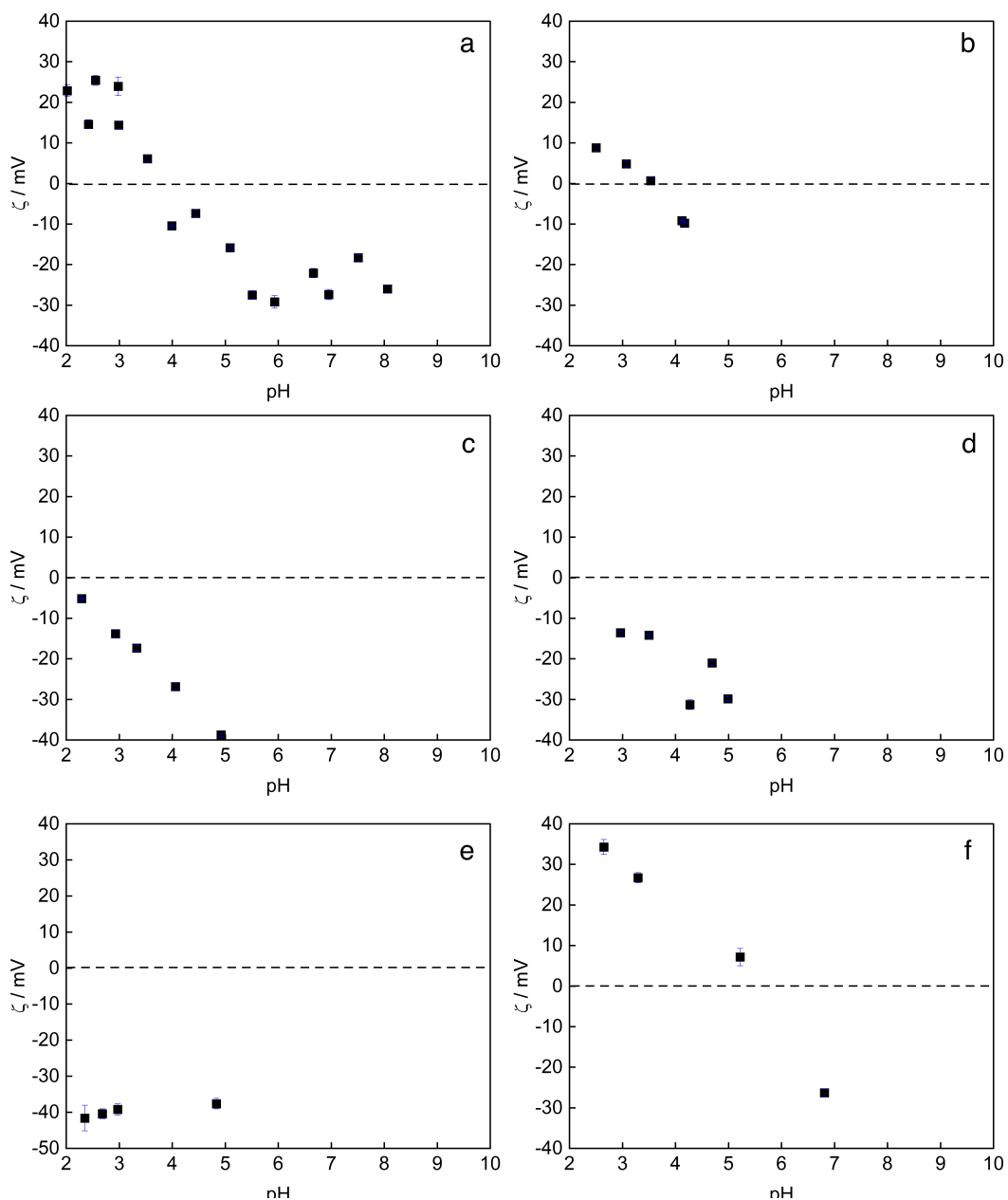
Figure 4. Experimental electrokinetic (ζ) potential measured at constant ionic strength $I = 10^{-2}\,\mathrm{mol\,L^{-1}}$ using the laser doppler microelectrophoretic method. (**a**) Ti$_{0.999}$W$_{0.001}$O$_2$N$_x$; (**b**) Ti$_{0.990}$W$_{0.010}$O$_2$N$_x$; (**c**) Ti$_{0.980}$W$_{0.020}$O$_2$N$_x$; (**d**) Ti$_{0.950}$W$_{0.050}$O$_2$N$_x$; (**e**) Ti$_{0.909}$W$_{0.091}$O$_2$; (**f**) TiO$_2$N$_x$.

5. Discussion

5.1. Nature of the Surface W Species

HAADF aberration-corrected STEM images of Ti$_{0.909}$W$_{0.091}$O$_2$N$_x$ (and our previous neutron diffraction/XPS work [31]) have confirmed the presence of W enriched non-crystalline clusters on the surface of anatase Ti$_{0.909}$W$_{0.091}$O$_2$N$_x$ nanoparticles beside a significant level of W and N inclusion in the nanoparticles crystal lattice. Charge compensation of the extra positive charges brought by W^{6+} when substituting for Ti^{4+} in the TiO$_2$ crystal lattice can occur via an increase of Ti^{4+} vacancies as well as an excess of electrons [32,58]. The latter induces a noticeable increase in the donor density of the materials [32], making

$Ti_{0.909}W_{0.091}O_2N_x$ even more n-type than undoped TiO_2. EPR then revealed that the non-crystalline W clusters on the surface of the nanoparticles are W_xO_y clusters and domains of W bronze-like superstructure. This was afforded via the detection of reduced W^{5+} species (most likely due to majority carriers trapping) in two distinct oxygen-coordinating environments, which highlights the unique ability of EPR in ascertaining the chemical nature of discrete motifs and supramolecular arrangements in the solid state, where other techniques (i.e., x-ray/neutron diffraction) would fail. In addition, a careful simulation of the intensities of the EPR resonances associated with these reduced W^{5+} species revealed that within the W_xO_y clusters and W bronzes-like superstructure, although not crystalline, a local order does exists, requiring the use of a suitable ordering potential λ (Equation (34)) for a correct simulation. According to the formalism adopted (Equations (33) and (34)), allowed values for λ are $-10 \leqslant \lambda \leqslant +10$. When λ is negative, the orientational distribution function $P(\theta)$ is maximum at $\theta = 90°$, indicating a preferential orientation of the molecular z axis perpendicular to the externally applied magnetic field (i.e., preferential alignment in the molecular xy plane); when λ is positive, the orientational distribution function $P(\theta)$ is maximum at $\theta = 0°$ and 180°, indicating a preferential orientation of the molecular z axis along the externally applied magnetic field. As the **g** tensor frame in our simulation was taken collinear to the molecular frame of reference, this value of λ implies that the **g** tensors of the electron spins show a preferential orientation with their z axis along the external magnetic field. This is evident in the red simulation which shows a greater relative contribution of the parallel components of **g** with respect to the perpendicular ones when compared to the powder simulation in blue where all orientations occur with the same probability. Furthermore, as the orientational distribution becomes sharper as the magnitude of λ increases, a value of 3 on a scale out of 10, represents a relatively significant orientational bias for the non-crystalline clusters in the limits of a powder sample approximation (i.e., where the orientational dependence is not resolved). There might be different reasons for this preferential orientational distribution, including a preferential growth of these clusters during nanoparticles synthesis. Another interesting features of these non-crystalline surface W clusters is that, despite the significant level of N doping in the sample, no sign of superhyperfine interaction between the unpaired electron in W^{5+} and the ^{14}N nuclei was detected. A potential explanation for this is that there is no N incorporated in these W_xO_y clusters and W bronzes-like superstructures, and all the N remains inside the crystalline anatase $Ti_{0.909}W_{0.091}O_2N_x$ phase. In fact, no hyperfine interaction to the only magnetic isotope of W, i.e., ^{183}W was detected in these clusters either, although this is most likely due to its low natural abundance in conjunction with the very low EPR signal intensity. On the contrary, the paramagnetic $N_iO^{\bullet}$ species arising from N doping in the anatase $Ti_{0.909}W_{0.091}O_2N_x$ phase, did indeed show superhyperfine coupling to the ^{183}W nucleous (W-NO^{2-} in Figure 2c), owing to the much greater EPR signal intensity and the vicinity of substitutional W. In the $Ti_{0.909}W_{0.091}O_2N_x$ phase, EPR failed to detect any substitutional W^{5+}. To the best of our knowledge, substitutional W^{5+} [59] has never been observed in anatase nanoparticles. On the contrary, substitutional W^{5+} has been detected in rutile or mixed anatase-rutile nanoparticles [59], signifying that the presence of rutile phases might be necessary to generate a stable form of reduced W^{5+} substituting for Ti^{4+}. The presence of reduced paramagnetic species induced by charge compensation following W doping can therefore be exploited by EPR as a valuable "probe" to ascertain details about surface species/clusters/phase-modifying domains contributing to dictate the surface chemistry of doped TiO_2 nanoparticles.

5.2. Dopant-Induced Surface Acidity

On the basis of the extensive degree of W-containing, surface covering clusters and the high level of substitutional W doping (both bulk and surface), and considering the much harder character of W^{6+} when compared to Ti^{4+} (W^{6+} has almost identical ionic radius as Ti^{4+}, i.e., 74 pm vs. 74.5 pm, respectively, but much greater Pauli electronegativity, i.e., 2.36 compared to 1.54), one would infer that hydrated $Ti_{0.909}W_{0.091}O_2N_x$ surfaces

would exhibit a much more acidic character than undoped TiO_2. As is evident from the surface charge density profiles and the pK_as values extracted from simulations, the effect of the doping is indeed to shift the protonation/deprotonation equilibria of the surface SOH of $Ti_{0.909}W_{0.091}O_2N_x$ towards much lower pH when compared to undoped TiO_2. It also corroborates an early measurement of increased acidity of WOx-TiO_2 surfaces by Li et al. [60]. In the case of undoped TiO_2, simulations of the $\sigma_0(pH)$ trends, returned (within experimental and calculation errors) the same values of the acidity constants pK_{a1}^{int} and pK_{a2}^{int} of surface sites (Table 3) proposed by Piasecki et al. [38] (despite using NaCl rather than $NaNO_3$ as in the present work). The formation and dissociation constants of the surface site complexes with cations and anions pK_C^{int} and pK_A^{int} also match very well what was previously proposed [38]. The formation reaction for SO^-C^+ has been already provided by Equation (15) with equilibrium constant defined according to Equation (19). The formation reaction for $SOH_2^+A^-$ can be seen as Equation (1) minus Equation (4), which implies an equilibrium constant equal to

$$K'_A = \frac{K_{a1}^{int}}{K_A^{int}} \tag{36}$$

Equation (36) returns a value for $K'_A = 2.24 \times 10^2 = K_C$, i.e., a symmetric association of counterions condition is proven. The symmetric association condition imposes that the value of pH_{pzc} corresponds to the state in which all electrical properties disappear, i.e., a true electroneutrality point: $\sigma_0 = \sigma_s = 0$ and $\psi_0 = \psi_d = \zeta = 0$, so that $pH_\infty = pH_{pzc} = pH_{iep} = pH_{pzp} = pH_{eln}$, where pH_{iep} is the iso-electric point, i.e., the pH at which $\zeta = 0$, pH_{pzp} the pH of zero (surface) potential and pH_{eln} the pH of electroneutrality. This is corroborated by the $\zeta(pH)$ trend (experimental laser Doppler micro-electrophoresis and simulation) reported in Figure 3f, showing a $pH_{iep} = 6$. We believe that the overestimation observed when using the acoustic method is due to the accuracy of the method, given that a value of 6.8 is significantly higher than what is normally reported in the literature for water suspensions of undoped TiO_2 in the presence of indifferent electrolyte only (as in this case). The situation for the $Ti_{0.909}W_{0.091}O_2N_x$ colloidal nanoparticles is however quite different. Suspensions of these in $I = 10^{-2}\,mol\,L^{-1}$ aqueous solutions with $NaNO_3$ as a supporting electrolyte revealed that $pH_{pzc} \neq pH_{iep}$, as evident from the comparison between Figure 2e,f. While the pH_{pzc} can still be obtained by the mass titration method also in the case of asymmetrical association of counterions [43], it is now expected to be shifted from the pH of electroneutrality pH_{eln}. By applying the same rationale as for undoped TiO_2 to $Ti_{0.909}W_{0.091}O_2N_x$, the formation constants for the surface site complexes with the counterions are now $K_C = 3.16 \times 10^2$ and $K'_A = 3.16 \times 10^4$, which would indicate a significant preferential association of anions, i.e., NO_3^-, over cations, i.e., Na^+. In this condition, the expectation is that pH_{pzc} is shifted from the pH_{eln} to a higher pH value, $pH_{pzc} > pH_{eln}$, while the pH_{iep} is shifted to a lower pH value with respect to pH_{eln}, $pH_{iep} < pH_{eln}$ (the point of zero potential pH_{pzp} remains close to pH_{eln}). This is in agreement with the experimental $\zeta(pH)$ indicating a $pH_{iep} < 1$. Furthermore, $\zeta(pH)$ trend and $pH_{iep} < 1$ are corroborated by what reported for WO_3 [61,62].

5.3. Single Contributions of W and N Dopants on Surface Acidity

EPR, microscopy and surface charge/electrokinetic results demonstrate that a W loading of ~10 at.% in TiO_2 generates nanoparticles with surface chemistry more similar to that of WO_3 than that of TiO_2, although maintaining the anatase crystal lattice typical of TiO_2. In this regards, EPR and microscopy shed light on the chemical and crystallographic nature of the surface, including the W clusters coverage, which is a fundamental starting point to understand the TLM properties and the electrophoretic behaviour observed once the particles are in contact with an aqueous electrolyte solution. As the W content was reduced, we observed a gradual increase of the pH_{iep} towards that of undoped TiO_2, as evident from the $\zeta(pH)$ curves in Figure 4a–d. Investigation of monodoped nanoparticles

further confirmed the influence of W and N on the surface chemistry. In the case of solely W doping with ~10.0 at.% W doping, we obtained similar W^{5+} EPR spectra (not shown here) and comparable $\zeta(pH)$ behaviour (Figure 4e) to that of $Ti_{0.909}W_{0.091}O_2N_x$. In the case of solely N doping (Figure 4f), the $\zeta(pH)$ profile was found almost identical as the one of undoped TiO_2. It therefore appears that the shift of the pH_{iep} is attributable to W doping only. On one hand, this is perfectly in line with what is discussed above related to the acidity of hydrated surface tungsten species. On the other hand, these results help to understand the role of interstitial N doping as a contributor to the overall surface chemistry observed. Xu et al. [9] reported a $\zeta(pH)$ profile that was unchanged with respect to undoped TiO_2; exactly as we are reporting here. In Xu et al. [9] and in the present work, N was introduced via a wet chemistry route (sol–gel) with subsequent annealing in air. As per our EPR data above, other EPR works of ours [30,31] and other groups [5,9] have shown this procedure predominantly generates Ti-ON-Ti adducts, where the nitrogen is found in interstitial positions bound to lattice oxygen. It therefore appears that this doping arrangement is not altering significantly the acidic character of surface TiOH groups as evidenced by an unchanged pH_{iep} for the N-doped TiO_2 with no W. Note though that Miyauchi et al. [63] found a pH_{iep} between pH 0 and 1 for N doped TiO_2 nanoparticles. Miyauchi et al. [63] however prepared their specimen through high temperature nitridation (annealing TiO_2 in the presence of NH_3 at 600 °C), a synthetic route known to induce prevalently the substitution of lattice O with N, i.e., Ti-N-Ti. If substituting a surface oxygen, N can form surface N-H groups which Brœnsted acidity is higher than surface O-H groups (N less electronegative than O, thus Ti-N bonding more covalent than Ti-O bonding, i.e., N-H bonding weaker than O-H bonding).

5.4. Overall Applicability of the Proposed Approach

A final note should be made regarding the applicability and limitations of the solid/water interface model adopted here. The 2-pK charging TLM model has proved to be a useful approach to interpret the chemistry of doped TiO_2/water interfaces, besides its already known validity for undoped single metal oxide/water interfaces. Nevertheless, if applying this model, one should always be mindful of its limitations. First, the model considers one single coordination type of surface site and does not discriminate amongst sites with different oxygen–metal coordination geometries, i.e., does not differentiate amongst terminal OH groups, bridging OH groups and adducts formed by non-dissociative adsorption of water molecules (see Folli et al. [64] for speciation, interconversion and stability of these different types of surface OH groups in anatase TiO_2). Second, the theoretical description of the 2-pK charging TLM model, considers H^+ as the potential-determining ion; however, it does not take into account possible intercalation of H^+ in the crystal structure. TiO_2 is commonly used in Li-ion batteries as Li^+ intercalates very well in the crystal lattice. Protons are even smaller than Li^+, therefore one should expected a non-negligible degree of intercalation for H^+, which implies that not all of the H^+ taken from the bulk of the electrolyte solution contribute to determining the surface potential according to Equations (1)–(4). This could be even more of a problem when considering $Ti_{0.909}W_{0.091}O_2N_x$ colloidal nanoparticles. Our EPR results highlighted the presence of W bronze-like surface superstructures on the surface of the doped anatase nanoparticles. W bronzes are well known for intercalating H^+ when W^{6+} reduces to W^{5+}, compensating the extra negative charge associated with the reduction event. As a result, there is the possibility that not all the H^+ available play a surface potential determining role. Therefore, the absolute values of the acidity and complexation constants derived by simulating the surface charge density data (in particular for the case of doped nanoparticles) should be treated cautiously. As to the latter point, the solid–water interface of W doped TiO_2 is (microscopically) characterised by WO^- and TiO^- sites reacting with the potential determining ions (i.e., H^+), where the boundary limits represent the surface of undoped TiO_2 in one case and the surface of WO_3 in the other. The 2-pK charging TLM model, as applied for the doped TiO_2 in the context of this work, does not discriminate between these sites but simply considers an

overall surface as if it was characterised by one type of surface sites SO$^-$ with overall acidity and counterion association constants equal to $K_{a1}^{int}, K_{a2}^{int}, K_C^{int}, K_A^{int}$. As a result, while the K_as for TiO$_2$ represents (within the limits described above about surface sites of different oxygen–metal coordination geometries) chemically specific acidity and counterion association constants of surface TiO$^-$ sites, in the case of the doped nanoparticles, the values reflect macroscopic averages of the entire surface. Nevertheless, these are still informative when it comes to understand and predict the surface adsorption modes of substrates undergoing photocatalytic conversion. A typical example is the degradation of zwitterionic dyes. It has been shown that at 4 <pH< 6 Rhodamine B adsorbs on the surface of TiO$_2$/SiO$_2$ particles via the positively charged diethylamino group rather than the negatively charged carboxyl group as expected on the surface of unmodified TiO$_2$ [65]. Similar results were obtained with TiO$_2$ nanoparticles where surface OH were replaced by F [66]. The intimate mix of the two oxides (i.e., TiO$_2$ and SiO$_2$) or the surface fluorination allowed for a significant drop of the pH$_{iep}$ and a predominantly negatively charged oxide surface, in a very similar fashion as the W doping in the present study. Interestingly, the mechanism of photocatalytic Rhodamine B degradation was observed to be dependent on the way Rhodamine B adsorbs on the surface of the photocatalyst [65,66]. These findings in conjunction with the evidence provided by this work, showing that even low levels of W doping cause a significant change of the photocatalyst surface chemistry, demonstrate that the comparison of photocatalytic activities of doped vs. undoped TiO$_2$ cannot be carried out based on light harvesting and band structure exclusively. A clear understanding of the photocatalyst surface chemistry driving adsorption/desorption events needs to be in place.

6. Conclusions

A combination of EPR, microscopy, electrophoresis and simulations to study the surface chemistry of doped TiO$_2$ photocatalysts is proposed. We show that EPR, coupled to other analytical methods, can be a powerful technique for elucidating the surface nature and chemistry of transition metal oxides. The study has focused on the case of W- and N-doped TiO$_2$. Using paramagnetic interstitial N centres and W^{5+} as spin probes, EPR and microscopy allowed to identify the chemical and crystallographic nature of the doped TiO$_2$ nanoparticles surface. In the case of high levels of W doping (9 to 10 at.%) the typical anatase surface modified by substitutional W was found to coexist with locally ordered W$_x$O$_y$ and W bronze-like clusters preferentially grown during synthesis. In addition, mass titration, surface charge density/potential and zeta potential measurements/simulations revealed, that at these levels of W doping, the surfaces of W and N codoped TiO$_2$ and W-doped TiO$_2$ are significantly more acidic when compared to their undoped TiO$_2$ counterparts; as revealed by the pH$_{pzc}$ and pH$_{iep}$ which were found to be comparable with those of WO$_3$ [61,62]. The results of our investigation also helped to understand the single role of nitrogen and tungsten as dopants on the anatase TiO$_2$/electrolyte solution interface. The presence of interstitial N did not alter the ordinary surface chemistry typical of undoped TiO$_2$ as confirmed by a ζ profiles for solely (interstitial) N doped TiO$_2$ which were found to be almost identical as the one obtained for undoped titania. On the contrary, W dramatically altered this chemistry. Lattice W^{6+} cations, as well as W containing clusters, generate very acidic surface W-OH groups compared to amphoteric Ti-OH. As a result, W has the major effect of changing the surface chemistry of TiO$_2$ whereas interstitial N seems to have no effect at all. Having identified how the TiO$_2$/electrolyte interface chemistry is modified as a consequence of doping with W and N and having provided tools for analysing these changes, this work adds to our existing knowledge of W and N doped TiO$_2$ photocatalytic activities and selectivities by providing important details that aid the interpretation and understanding of adsorption/desorption mechanisms of species that are transformed during photocatalytic events.

10^{-2} mol L^{-1}. Two titrations (alkaline runs) were performed starting at a pH farer (black markers) and closer (blue markers) to the expected pH of zero charge pH$_{pzc}$. The starting pH was obtained adding a a 0.1 mol L^{-1} solution of NaOH, Figure S2: Mass titration of undoped anatase TiO$_2$ in deionised water and NaNO$_3$ as a supporting electrolyte to adjust the ionic strength at the constant value of $I = 10^{-2}$ mol L^{-1}. The decaying curve represents the alkaline run (starting pH obtained adding a 0.1 mol L^{-1} solution of NaOH) whilst the growing curve represents the acidic run (starting pH obtained adding a 0.1 mol L^{-1} solution of HNO$_3$), Figure S3: Titration for the determination of the degree of contamination u for the undoped anatase TiO$_2$ used in this work. Reference [67] is cited in the supplementary materials.

References

1. Folli, A.; Bloh, J.Z.; Strøm, M.; Pilegaard Madsen, T.; Henriksen, T.; Macphee, D.E. Efficiency of Solar-Light-Driven TiO$_2$ Photocatalysis at Different Latitudes and Seasons. Where and When Does TiO$_2$ Really Work? *J. Phys. Chem. Lett.* **2014**, *5*, 830–832.
2. Liu, L.; Chen, X. Titanium Dioxide Nanomaterials: Self-Structural Modifications. *Chem. Rev.* **2014**, *114*, 9890–9918.
3. Zuo, F.; Bozhilov, K.; Dillon, R.J.; Wang, L.; Smith, P.; Zhao, X.; Bardeen, C.; Feng, P. Active Facets on Titanium(III)-Doped TiO2: An Effective Strategy to Improve the Visible-Light Photocatalytic Activity. *Angew. Chem.* **2012**, *124*, 6327–6330.
4. Xing, M.; Li, X.; Zhang, J. Synergistic effect on the visible light activity of Ti3+ doped TiO$_2$ nanorods/boron doped graphene composite. *Sci. Rep.* **2014**, *4*, 1–7.
5. Livraghi, S.; Paganini, M.C.; Giamello, E.; Selloni, A.; Di Valentin, C.; Pacchioni, G. Origin of Photoactivity of Nitrogen-Doped Titanium Dioxide under Visible Light. *J. Am. Chem. Soc.* **2006**, *128*, 15666–15671.
6. Chen, X.; Burda, C. The Electronic Origin of the Visible-Light Absorption Properties of C-, N- and S-Doped TiO$_2$ Nanomaterials. *J. Am. Chem. Soc.* **2008**, *130*, 5018–5019.
7. Czoska, A.M.; Livraghi, S.; Paganini, M.C.; Giamello, E.; Di Valentin, C.; Pacchioni, G. The nitrogen-boron paramagnetic center in visible light sensitized N-B co-doped TiO$_2$. Experimental and theoretical characterization. *Phys. Chem. Chem. Phys.* **2011**, *13*, 136–143.
8. Barolo, G.; Livraghi, S.; Chiesa, M.; Paganini, M.C.; Giamello, E. Mechanism of the Photoactivity under Visible Light of N-Doped Titanium Dioxide. Charge Carriers Migration in Irradiated N-TiO$_2$ Investigated by Electron Paramagnetic Resonance. *J. Phys. Chem. C* **2012**, *116*, 20887–20894.
9. Xu, J.; Wang, F.; Liu, W.; Cao, W. Nanocrystalline N-Doped TiO$_2$ Powders: Mild Hydrothermal Synthesis and Photocatalytic Degradation of Phenol under Visible Light Irradiation. *Int. J. Photoenergy* **2013**, *2013*, 1–7.
10. Yuan, W.; Li, J.; Wang, L.; Chen, P.; Xie, A.; Shen, Y. Nanocomposite of N-Doped TiO$_2$ Nanorods and Graphene as an Effective Electrocatalyst for the Oxygen Reduction Reaction. *ACS Appl. Mater. Interfaces* **2014**, *6*, 21978–21985.
11. Bauer, D.; Roberts, A.J.; Matsumi, N.; Darr, J.A. Nano-sized Mo- and Nb-doped TiO$_2$ as anode materials for high energy and high power hybrid Li-ion capacitors. *Nanotechnology* **2017**, *28*, 195403.
12. Chang, T.T. Paramagnetic Resonance Spectrum of W5+ in Rutile (TiO$_2$). *Phys. Rev.* **1966**, *147*, 264–267.
13. De Trizio, L.; Buonsanti, R.; Schimpf, A.M.; Llordes, A.; Gamelin, D.R.; Simonutti, R.; Milliron, D.J. Nb-Doped Colloidal TiO$_2$ Nanocrystals with Tunable Infrared Absorption. *Chem. Mater.* **2013**, *25*, 3383–3390.
14. Nosaka, Y.; Takahashi, S.; Sakamoto, H.; Nosaka, A.Y. Reaction Mechanism of Cu(II)-Grafted Visible-Light Responsive TiO$_2$ and WO3 Photocatalysts Studied by Means of ESR Spectroscopy and Chemiluminescence Photometry. *J. Phys. Chem. C* **2011**, *115*, 21283–21290.
15. Yang, Y.; Wang, H.; Li, X.; Wang, C. Electrospun mesoporous W6+-doped TiO$_2$ thin films for efficient visible-light photocatalysis. *Mater. Lett.* **2009**, *63*, 331–333.
16. Zimmermann, P.H. Temperature Dependence of the EPR Spectra of Niobium-Doped TiO$_2$. *Phys. Rev. B* **1973**, *8*, 3917–3927.
17. Yue, J.; Suchomski, C.; Voepel, P.; Ellinghaus, R.; Rohnke, M.; Leichtweiss, T.; Elm, M.T.; Smarsly, B.M. Mesoporous niobium-doped titanium dioxide films from the assembly of crystalline nanoparticles: study on the relationship between the band structure, conductivity and charge storage mechanism. *J. Mater. Chem. A* **2017**, *5*, 1978–1988.
18. Atashbar, M.Z.; Sun, H.T.; Gong, B.; Wlodarski, W.; Lamb, R. XPS study of Nb-doped oxygen sensing TiO$_2$ thin films prepared by sol-gel method. *Thin Solid Films* **1998**, *326*, 238–244.

19. Tobaldi, D.M.; Pullar, R.C.; Gualtieri, A.F.; Seabra, M.P.; Labrincha, J.A. Sol-gel synthesis, characterisation and photocatalytic activity of pure, W-, Ag- and W/Ag co-doped TiO_2 nanopowders. *Chem. Eng. J.* **2013**, *214*, 364–375.

20. Tasaki, C.; Oka, N.; Yagi, T.; Taketoshi, N.; Baba, T.; Kamiyama, T.; Nakamura, S.-I.; Shigesato, Y. Thermophysical Properties of Transparent Conductive Nb-Doped TiO_2 Films. *Jpn. J. App. Phys.* **2012**, *51*, 035802.

21. Lee, S.; Noh, J.H.; Han, H.S.; Yim, D.K.; Kim, D.H.; Lee, J.-K.; Kim, J.Y.; Jung, H.S.; Hong, K.S. Nb-Doped TiO_2: A New Compact Layer Material for TiO_2 Dye-Sensitized Solar Cells. *J. Phys. Chem. C* **2009**, *113*, 6878–6882.

22. Lee, H.Y.; Robertson, J. Doping and compensation in Nb-doped anatase and rutile TiO_2. *J. App. Phys.* **2013**, *113*, 213706.

23. Couselo, N.; GarciaEinschlag, F.; Candal, R.; Jobbagy, M. Tungsten-Doped TiO_2 vs. Pure TiO_2 Photocatalysts: Effects on Photobleaching Kinetics and Mechanism. *J. Phys. Chem. C* **2008**, *112*, 1094–1100.

24. Tung, W.S.; Daoud, W.A. New Approach Toward Nanosized Ferrous Ferric Oxide and Fe_3O_4-doped Titanium Dioxide Photocatalysts. *ACS Appl. Mater. Interfaces* **2009**, *1*, 2453–2461.

25. Thind, S.S.; Wu, G.; Chen, A. Synthesis of mesoporous nitrogen–tungsten co-doped TiO_2 photocatalysts with high visible light activity. *Appl. Catal. B Environ.* **2012**, *111–112*, 38–45.

26. Çelik, V.; Mete, E. Range-separated hybrid exchange-correlation functional analyses of anatase TiO_2 doped with W, N, S, W/N, or W/S. *Phys. Rev. B* **2012**, *86*, 205112.

27. Biedrzycki, J.; Livraghi, S.; Giamello, E.; Agnoli, S.; Granozzi, G. Fluorine- and Niobium-Doped TiO_2: Chemical and Spectroscopic Properties of Polycrystalline n-Type-Doped Anatase. *J. Phys. Chem. C* **2014**, *118*, 8462–8473.

28. Kubacka, A.; Colón, G.; Fernández-García, M. N- and/or W-(co)doped TiO_2-anatase catalysts: Effect of the calcination treatment on photoactivity. *Appl. Catal. B* **2010**, *95*, 238–244.

29. Sajjad, A. K.L.; Shamaila, S.; Zhang, J. Study of new states in visible light active W, N co-doped TiO_2 photo catalyst. *Mater. Res. Bull.* **2012**, *47*, 3083–3089.

30. Folli, A.; Bloh, J.Z.; Beukes, E.P.; Howe, R.F.; Macphee, D.E. Photogenerated Charge Carriers and Paramagnetic Species in (W,N)-Codoped TiO_2 Photocatalysts under Visible-Light Irradiation: An EPR Study. *J. Phys. Chem. C* **2013**, *117*, 22149–22155.

31. Folli, A.; Bloh, J.Z.; Armstrong, K.; Richards, E.; Murphy, D.M.; Lu, L.; Kiely, C.J.; Morgan, D.J.; Smith, R.I.; Mclaughlin, A.C.; et al. Improving the Selectivity of Photocatalytic NOx Abatement through Improved O_2 Reduction Pathways Using Ti0.909W0.091O2Nx Semiconductor Nanoparticles: From Characterization to Photocatalytic Performanc. *ACS Catal.* **2018**, *8*, 6927–6938.

32. Bloh, J.Z.; Folli, A.; Macphee, D.E. Adjusting Nitrogen Doping Level in Titanium Dioxide by Codoping with Tungsten: Properties and Band Structure of the Resulting Materials. *J. Phys. Chem. C* **2014**, *118*, 21281–21292.

33. Folli, A.; Bloh, J.Z.; Walker, R.; Lecaplain, A.; Macphee, D.E. Properties and Photochemistry of Valence-Induced-Ti3+ Enriched (Nb,N)-Codoped Anatase TiO_2 Semiconductors. *Phys. Chem. Chem. Phys.* **2015**, *17*, 4849–4853.

34. Borlaf, M.; Colomer, M.T.; De Andrés, A.; Cabello, F.; Serna, R.; Moreno, R. TiO_2/Eu3+ thin films with high photoluminescence emission prepared by electrophoretic deposition from nanoparticulate sols. *Eur. J. Inorg. Chem.* **2014**, *2014*, 5152–5159.

35. us Saqib, N.; Adnan, R.; Shah, I. A mini-review on rare earth metal-doped TiO_2 for photocatalytic remediation of wastewater. *Environ. Sci. Pollut. Res.* **2016**, *23*, 15941–15951.

36. D' Arienzo, M.; Siedl, N.; Sternig, A.; Scotti, R.; Morazzoni, F.; Bernardi, J.; Diwald, O. Solar light and dopant-induced recombination effects: Photoactive nitrogen in TiO_2 as a case study. *J. Phys. Chem. C* **2010**, *114*, 18067–18072.

37. Blesa, M.A.; Kallay, N. The metal oxide - electrolyte solution interface revisited. *Adv. Colloid Interf. Sci.* **1988**, *28*, 111–134.

38. Piasecki, W.; Rudzinski, W.; Charmas, R. 1-p K and 2-p K Protonation Models in the Theoretical Description of Simple Ion Adsorption at the Oxide/Electrolyte Interface: A Comparative Study of the Behavior of the Surface Charge, the Individual Isotherms of Ions, and the Accompanying Electrokinetic. *J. Phys. Chem. B* **2001**, *105*, 9755–9771.

39. Tejedor-Tejedor, M.I.; Anderson, M.A. In situ attenuated total reflection fourier transform infrared studies of the Goethite (alpha-FeOOH)-acqueous solution interface. *Langmuir* **1986**, *2*, 203–210.

40. Macphee, D.E.; Bloh, J.Z.; Folli, A.; Greenhalgh, D. A method of photocatalytically oxidising nitrogen oxides. Patent WO/2016/005760A1, 14 January 2016.

41. Stoll, S.; Schweiger, A. EasySpin, a Comprehensive Software Package for Spectral Simulation and Analysis in EPR. *J. Magn. Reson.* **2006**, *178*, 42–55.

42. Folli, A.; Pochard, I.; Nonat, A.; Jakobsen, U.; Shepherd, A.; Macphee, D. Engineering photocatalytic Cements: Understanding TiO_2 surface chemistry to control and modulate photocatalytic performances. *J. Amer. Ceram. Soc.* **2010**, *93*, 3360–3369.

43. Preocanin, T.; Kallay, N. Point of zero charge and surface charge density of TiO_2 in aqueous electrolyte solution as obtained by potentiometric mass titration. *Croat. Chem. Acta* **2006**, *79*, 95–106.

44. Reymond, J.P.; Kolenda, F. Estimation of the point of zero charge of simple and mixed oxides by mass titration. *Powder Tech.* **1999**, *103*, 30–36.

45. Zalac, S.; Kallay, N. Application of Mass Titration to the Point of Zero Charge Determination. *J. Colloid Interf. Sci.* **1992**, *149*, 233–240.

46. Di Valentin, C.; Finazzi, E.; Pacchioni, G.; Selloni, A.; Livraghi, S.; Paganini, M.C.; Giamello, E. N-doped TiO_2: Theory and Experiment. *Chem. Phys.* **2007**, *339*, 44–56.

47. Livraghi, S.; Chierotti, M.R.; Giamello, E.; Magnacca, G.; Paganini, M.C.; Cappelletti, G.; Bianchi, C.L. Nitrogen-Doped Titanium Dioxide Active in Photocatalytic Reactions with Visible Light: A Multi-Technique Characterization of Differently Prepared Materials. *J. Phys. Chem. C* **2008**, *112*, 17244–17252.

48. Messai, Y.; Vileno, B.; Martel, D.; Turek, P.; Mekki, D.E. Milling effect on the photo-activated properties of TiO$_2$ nanoparticles: Electronic and structural investigations. *Bull. Mater. Sci.* **2018**, *41*, 1–11.

49. Kuba, S.; Heydorn, P.; Grasselli, R.K.; Gates, B.C.; Chec, M.; Kno, H. Redox Properties of Tungstated Zirconia Catalysts : Relevance to the Activation of n-Alkanes. *Phys. Chem. Chem. Phys.* **2001**, *3*, 146–154.

50. Occhiuzzi, M.; Cordischi, D.; De Rossi, S.; Ferraris, G.; Gazzoli, D.; Valigi, M. Pd-Promoted WO$_x$/ZrO$_2$ Catalysts: Characterization and Catalytic Activity for n-Butane Isomerization. *Appl. Catal. A* **2008**, *351*, 29–35.

51. Occhiuzzi, M.; Cordischi, D.; Gazzoli, D.; Valigi, M.; Heydorn, P.C. WO$_x$/ZrO2 Catalysts Part 4. Redox Properties as Investigated by Redox Cycles, XPS and EPR. *Appl. Catal. A* **2004**, *269*, 169–177.

52. Weil, J.A.; Bolton, J.R.; Wertz, J.E. *Electron Paramagnetic Resonance: Elementary Theory and Practical Applications*, 1st ed.; John Wiley & Sons: New York, NY, USA, 1994; p. 568.

53. Castner, T.; Newell, G.S.; Holton, W.C.; Slighter, C.P. Note on the paramagnetic resonance of iron in glass. *J. Chem. Phys.* **1960**, *32*, 668–673.

54. Howe, R.F.; Gratzel, M. EPR observation of trapped electrons in colloidal titanium dioxide. *J. Phys. Chem.* **1985**, *89*, 4495–4499.

55. Micic, O.I.; Zhang, Y.; Cromack, K.R.; Trifunac, A.D.; Thurnauer, M.C. Photoinduced Hole Transfer from TiO$_2$ to Methanol Molecules in Aqueous Solution Studied by Electron Paramagnetic Resonance. *J. Phys. Chem.* **1993**, *97*, 13284–13288.

56. Micic, O.I.; Zhang, Y.; Cromack, K.; Trifunac, A.D.; Thurnauer, M.C. Trapped holes on TiO$_2$ colloids studied by electron paramagnetic resonance. *J. Phys. Chem.* **1993**, *97*, 7277–7283.

57. Jenkins, C.A.; Murphy, D.M. Thermal and photoreactivity of TiO$_2$ at the gas-solid interface with aliphatic and aromatic aldehydes. *J. Phys. Chem. B* **1999**, *103*, 1019–1026.

58. Fernandez-Garcia, M.; Martínez-Arias, A.; Fuerte, A.; Conesa, J.C. Nanostructured Ti-W Mixed-Metal Oxides: Structural and Electronic Properties. *J. Phys. Chem. B* **2005**, *109*, 6075–6083.

59. Spencer, J.; Folli, A.; Richards, E.; Murphy, D.M. Applications of electron paramagnetic resonance spectroscopy for interrogating catalytic systems. In *Electron Paramagnetic Resonance*; Chechik, V., Murphy, D.M., Eds.; Royal Society of Chemistry: Cambridge, UK, 2019; Volume 26; pp. 130–170.

60. Li, X.Z.; Li, F.B.; Yang, C.L.; Ge, W.K. Photocatalytic activity of WO$_x$-TiO$_2$ under visible light irradiation. *J. Photochem. Photobiol. A* **2001**, *141*, 209–217.

61. Park, H.; Yang, D.-J.; Yoo, J.-S.; Mun, K.-S.; Kim, W.-R.; Kim, H.-G.; Choi, W.-Y. Surface passivation of highly ordered TiO$_2$ nanotube arrays and application to dye-sensitized solar cells using the concept of isoelectric point. *J. Ceram. Soc. Japan* **2009**, *117*, 596–599.

62. Andersson, K.M.; Bergström, L. DLVO interactions of tungsten oxide and cobalt oxide surfaces measured with the colloidal probe technique. *J. Colloid Interf. Sci.* **2002**, *246*, 309–315.

63. Miyauchi, M.; Ikezawa, A.; Tobimatsu, H.; Irie, H.; Hashimoto, K. Zeta potential and photocatalytic activity of nitrogen doped TiO$_2$ thin films. *Phys. Chem. Chem. Phys.* **2004**, *6*, 865–870.

64. Folli, A.; Campbell, S.B.; Anderson, J.A.; Macphee, D.E. Role of TiO$_2$ Surface Hydration on NO Oxidation Photo-Activity. *J. Photochem. Photobiol. A* **2011**, *220*, 85–93.

65. Chen, F.; Zhao, J.; Hidaka, H. Highly selective deethylation of rhodamine B: Adsorption and photooxidation pathways of the dye on the TiO$_2$/SiO$_2$ composite photocatalyst. *Intern. J. Photoenergy* **2003**, *5*, 209–217.

66. Wang, Q.; Chen, C.; Zhao, D.; Ma, W.; Zhao, J. Change of Adsorption Modes of Dyes on Fluorinated TiO$_2$ and Its Effect on Photocatalytic Degradation of Dyes under Visible Irradiation. *Langmuir* **2008**, *24*, 7338–7345.

67. Sonnefeld, J. On the influence of background electrolyte concentration on the position of the isoelectric point and the point of zero charge. *Colloids Surfaces Physicochem. Eng. Asp.* **2001**, *190*, 179–183.